AGU PUBLICATIONS

JGR

Journal of Geophysical Research: Space Physics

RESEARCH ARTICLE
10.1002/2017JA024538

Special Section:
Magnetospheric Multiscale (MMS) mission results throughout the first primary mission phase

MMS Observations and Hybrid Simulations of Surface Ripples at a Marginally Quasi-Parallel Shock

Imogen Gingell[1], Steven J. Schwartz[1], David Burgess[2], Andreas Johlander[3], Christopher T. Russell[4], James L. Burch[5], Robert E. Ergun[6], Stephen Fuselier[5,7], Daniel J. Gershman[8], Barbara L. Giles[8], Katherine A. Goodrich[6], Yuri V. Khotyaintsev[3], Benoit Lavraud[9], Per-Arne Lindqvist[3], Robert J. Strangeway[4], Karlheinz Trattner[6], Roy B. Torbert[10], Hanying Wei[4], and Frederick Wilder[6]

[1]The Blackett Laboratory, Imperial College London, UK, [2]School of Physics and Astronomy, Queen Mary University of London, London, UK, [3]Swedish Institute of Space Physics (Uppsala), Uppsala, Sweden, [4]Department of Earth, Planetary and Space Physics, University of California, Los Angeles, CA, USA, [5]Southwest Research Institute, San Antonio, TX, USA, [6]Laboratory of Atmospheric and Space Sciences, University of Colorado Boulder, Boulder, CO, USA, [7]Department of Physics and Astronomy, University of Texas at San Antonio, San Antonio, TX, USA, [8]NASA, Goddard Space Flight Center, Greenbelt, MD, USA, [9]Institut de Recherche en Astrophysique et Planetologie, University de Toulouse, Toulouse, France, [10]Physics Department, University of New Hampshire, Durham, NH, USA

Key Points:
- A surface ripple has been observed by MMS at Earth's quasi-parallel bow shock
- Hybrid simulations show that these ripples are transients modulated by shock reformation
- Changes in the observed ripple are consistent with reformation processes

Correspondence to:
I. Gingell,
i.gingell@imperial.ac.uk

Citation:
Gingell, I., Schwartz, S. J., Burgess, D., Johlander, A., Russell, C. T., Burch, J. L., … Wilder, F. (2017). MMS observations and hybrid simulations of surface ripples at a marginally quasi-parallel shock. *Journal of Geophysical Research: Space Physics*, *122*. https://doi.org/10.1002/2017JA024538

Received 30 JUN 2017
Accepted 30 SEP 2017
Accepted article online 6 OCT 2017
Corrected 17 NOV 2017

This article was corrected on 17 NOV 2017. See the end of the full text for details.

©2017. The Authors.
This is an open access article under the terms of the Creative Commons Attribution License, which permits use, distribution and reproduction in any medium, provided the original work is properly cited.

Abstract Simulations and observations of collisionless shocks have shown that deviations of the nominal local shock normal orientation, that is, surface waves or ripples, are expected to propagate in the ramp and overshoot of quasi-perpendicular shocks. Here we identify signatures of a surface ripple propagating during a crossing of Earth's marginally quasi-parallel ($\theta_{Bn} \sim 45°$) or quasi-parallel bow shock on 27 November 2015 06:01:44 UTC by the Magnetospheric Multiscale (MMS) mission and determine the ripple's properties using multispacecraft methods. Using two-dimensional hybrid simulations, we confirm that surface ripples are a feature of marginally quasi-parallel and quasi-parallel shocks under the observed solar wind conditions. In addition, since these marginally quasi-parallel and quasi-parallel shocks are expected to undergo a cyclic reformation of the shock front, we discuss the impact of multiple sources of nonstationarity on shock structure. Importantly, ripples are shown to be transient phenomena, developing faster than an ion gyroperiod and only during the period of the reformation cycle when a newly developed shock ramp is unaffected by turbulence in the foot. We conclude that the change in properties of the ripple observed by MMS is consistent with the reformation of the shock front over a time scale of an ion gyroperiod.

1. Introduction

Collisionless shocks are found in many astrophysical plasma environments, such as planetary bow shocks, interplanetary shocks in the solar wind, and supernova remnants. These shocks are by necessity kinetic structures, for which particle processes play an important role in the dissipation of energy in the transition from supersonic to subsonic flow. One of the principal parameters in determining the shock physics is the angle between the shock normal and the upstream magnetic field, θ_{Bn}. A quasi-perpendicular shock has $\theta_{Bn} > 45°$, a quasi-parallel shock has $\theta_{Bn} < 45°$, and for this study we define a marginally quasi-parallel shock as one for which $\theta_{Bn} \sim 45°$. For both quasi-parallel and quasi-perpendicular shocks, the reflection of ions at the shock ramp is critical for understanding ion heating and acceleration (Gosling & Robson, 1985).

Microphysical processes are known to drive a variety of nonstationary processes which affect shock structure, introducing significant temporal and spatial variation at scales similar to and below the ion gyroscales. Given the dependence of shock physics on microscale processes, particularly in the cross-scale coupling of ion- and electron-driven phenomena, we expect shock nonstationarity to have a significant effect on energy dissipation and particle acceleration (Auer et al., 1962; Morse et al., 1972). For example, nonstationary processes in the shock transition region can modulate the injection of ions (Sundberg et al., 2016) and, therefore, affect the efficiency of a shock as a particle accelerator. This study will focus on two sources of nonstationarity in collisionless shocks: shock surface ripples, and cyclic reformation of the shock ramp.

Shock reformation is a process by which the short-scale shock ramp structure is periodically regenerated upstream of the shock. For quasi-perpendicular shocks, reformation can be driven by the reflected ion population (Biskamp & Welter, 1972; Hada et al., 2003; Scholer et al., 2003) or by instabilities associated with whistler waves localized in the foot region (Scholer & Burgess, 2007). For quasi-parallel shocks, reformation can be driven by instabilities of the backstreaming ion beam in the foreshock and steepening of upstream waves with shock-directed group velocity (Burgess, 1989, 1995; Krauss-Varban & Omidi, 1991). Reformation is therefore dependent on the solar wind plasma parameters such as the ion plasma beta, and shock parameters such as θ_{Bn}, the Mach number, and densities of the reflected and backstreaming ion populations (Burgess & Scholer, 2015). Evidence for shock reformation at Earth's quasi-perpendicular bow shock has been presented both statistically (Mazelle et al., 2010) and in detail for single shock crossings (Lobzin et al., 2007) using observations by the Cluster spacecraft.

Shock surface waves, also known as ripples, are periodic and propagating deviations in the nominal local shock normal orientation first identified in simulations of perpendicular shocks (Lowe & Burgess, 2003). These ripples can act as sites of electron acceleration (Umeda et al., 2009) and have been shown to influence the local ion dynamics (Hao et al., 2016; Yang et al., 2012). However, the underlying physical processes which lead to the growth of shock surface ripples are not yet understood. The length scales associated with ripples are short, typically on the order of a few ion inertial lengths. In combination with the need for multipoint spacecraft data, observations have therefore been limited. The first evidence for a rippled shock was presented by Moullard et al. (2006), who utilized a particularly slow crossing of Earth's bow shock by the Cluster spacecraft. More recently, Johlander et al. (2016) have utilized high-resolution particle and field data from the Magnetospheric Multiscale (MMS) mission (Burch et al., 2016) to reconstruct the form of a ripple on a relatively fast crossing of the Earth's bow shock. In both cases, the ripple was observed at a quasi-perpendicular bow shock. The MMS mission enables study of the ion and electron phase space at 2 orders of magnitude greater time resolution than the preceeding multispacecraft missions, Cluster and Time History of Events and Macroscale Interactions during Substorms. For this reason, it is ideal for the study of nonstationary structure such as ripples and shock reformation.

In this paper, we present evidence of a surface ripple observed by MMS. This is a phenomenon generally associated with quasi-perpendicular shocks but is observed here at a marginally quasi-parallel shock. To support these observations, we discuss a set of two-dimensional hybrid simulations of shocks of varying θ_{Bn} and show that quasi-parallel and marginally quasi-parallel shocks exhibit clear surface ripples only during certain periods of the reformation cycle. Using these simulations, we conclude that the observations are consistent with the occurrence of surface ripples modulated by cyclic reformation of the shock with a period similar to the time taken by the spacecraft to cross the shock.

2. Observations

2.1. Overview

We examine a crossing of Earth's bow shock by the four MMS spacecraft on 27 November 2015, 06:01:44 UTC. During this period, the mean spacecraft separation is 14 km. This shock crossing has been captured in burst mode, with magnetic field data provided by the FGM instrument (Russell et al., 2016) within the FIELDS instrument suite (Torbert et al., 2016). Ion and electron data have been provided by FPI-DIS and FPI-DES, respectively (Pollock et al., 2016). The full three-dimensional ion phase space is sampled by FPI-DIS every 0.15 s, and the electron phase space is sampled by FPI-DES every 0.03 s. The sampling frequency of the magnetic field data provided by the FGM instrument is 128 Hz.

An overview of the event is shown for MMS1 in Figure 1. The shock coordinate system we use in this figure, and subsequently in the analysis presented in the paper, is described by the shock normal unit vector $\hat{\mathbf{n}}$, and tangential unit vectors $\hat{\mathbf{t}}_1, \hat{\mathbf{t}}_2$, where $\hat{\mathbf{t}}_2 = \hat{\mathbf{n}} \times \mathbf{B}_u / B_u$ and $\hat{\mathbf{t}}_1 = \hat{\mathbf{t}}_2 \times \hat{\mathbf{n}}$. Hence, the upstream magnetic field $\mathbf{B}_u$ lies in the plane defined by vectors $\hat{\mathbf{t}}_1$ and $\hat{\mathbf{n}}$. In Figure 1, the magnetic time series demonstrate a transition from a turbulent, shocked plasma in the overshoot to a quiet upstream solar wind over a period of approximately 2 min.

The shock normal $\hat{\mathbf{n}}$ is determined by mixed method, using the magnetic field and electron bulk velocities upstream and downstream of the shock (Abraham-Shrauner, 1972; Schwartz, 1998). Given the turbulent and nonstationary nature of the shock transition layer and the associated differences in the shock profiles, determination of the shock normal and velocity by multiple spacecraft timing analysis is not considered reliable for determining the large-scale orientation of the shock. However, these methods will be employed

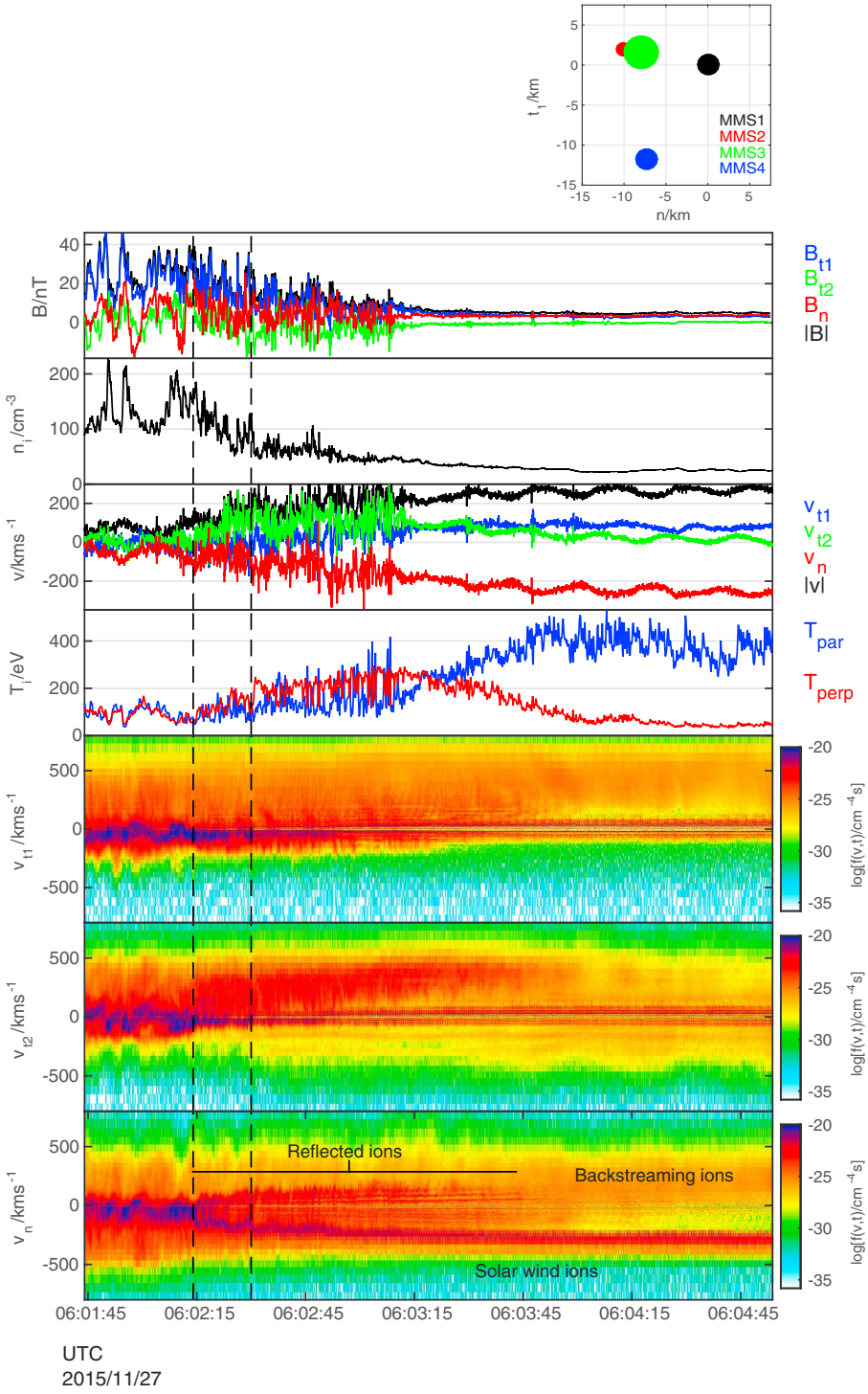


Figure 1. Overview of the full shock transition for the 27 November 2015 06:01:44 UTC event in the shock coordinate system as observed by MMS1. From top to bottom: spacecraft configuration (where marker size represents position in the t_2 coordinate), magnetic field components and magnitude, ion number density, bulk electron velocity components and magnitude, ion temperature moments, and the ion phase space densities as a function of the tangential and normal velocities, each integrated over the other two velocity components. Dashed lines mark the time interval shown in Figure 2.

Table 1
Shock and Solar Wind Parameters for the Marginally Quasi-Parallel Shock Crossing by MMS at 27 November 2015 06:01:44 UTC

Parameter	Value
Shock angle, θ_{Bn}	$43 \pm 3°$
Alfvén Mach number, M_A	11 ± 1
Fast magnetosonic Mach number, M_{fast}	~ 6
Shock normal (GSE), $\hat{\mathbf{n}}$	[0.98 −0.09 −0.15]
Solar wind magnetic field (GSE), $\mathbf{B}_{\text{sw}}$	[3.08 −1.80 −3.47] ±0.1 nT
Solar wind density, n_{sw}	26 ± 1 cm^{-3}
Solar wind velocity (GSE), $\mathbf{v}_{\text{sw}}$	[−255 12 −50] ±20 kms^{-1}
Upstream ion gyroperiod, $t_{\Omega,\text{sw}}$	13.2 ± 0.7 s
Upstream Alfvén speed, $v_{\text{A,sw}}$	21.8 ± 0.2 kms^{-1}
Overshoot Alfvén speed, $v_{\text{A,o}}$	100 ± 5 kms^{-1}
Solar wind ion plasma beta, β_i	2.0 ± 0.5

to determine local deviations of the shock normal later in this paper. The angle between the upstream magnetic field and the shock normal is found to be $\theta_{Bn} = 42°$, close to the $\theta_{Bn} \sim 47°$ predicted by employing a model of the bow shock (Peredo et al., 1995). We can estimate the shock speed using the crossing time of the shock foot according to the method outlined by Gosling and Thomsen (1985). For a foot crossing time of $\Delta t \sim 75$ s, the shock speed is given by $v_{\text{shock},n} \sim 2$ kms^{-1}.

The measured shock normal is within the idealized range for which the guiding center motion of specularly reflected ions is directed upstream, $\theta_{Bn} < 45°$, but specularly reflected ions will always reencounter the shock as they gyrate in the upstream magnetic field if $\theta_{Bn} > 39.9°$ (Schwartz et al., 1983). If transmission of particles is solely dependent upon the normal velocity, this marginally quasi-parallel range $39.9° < \theta_{Bn} < 45°$ represents a region for which ions may be reflected several times and thus remain in the vicinity of the shock for an extended period. In reality this range of angles is broadened by fluctuations in the shock layer and upstream field and by time-dependent processes such as shock reformation; a gradual change in shock properties in the transition from quasi-perpendicular to quasi-parallel geometry is expected. The Alfvén Mach number for this crossing, based on the upstream bulk velocity, is $M_A = 11$. Other shock and upstream solar wind parameters are summarized in Table 1. Upstream parameters are determined from the time interval 06:04:00 to 06:04:53 UTC, during which the upstream magnetic field is steady. Downstream parameters are determined from the time interval 06:01:44 to 06:02:04 UTC. The solar wind density and velocity moments for these periods are provided by the FPI-DES instrument. Since the FPI-DIS instrumentation is not designed to monitor the solar wind, the solar wind ion plasma β_i given in the table has been provided by NASA/GSFC's OMNI data set (King & Papitashvili, 2005).

The time series of the ion phase space densities as a function of the shock tangential and normal velocities, shown in Figure 1 (bottom), are calculated by integration of the full ion phase space density over the orthogonal directions, that is, $f(v_n, t) = \int f(v_{t1}, v_{t2}, v_n, t) \mathrm{d}v_{t1} \mathrm{d}v_{t2}$. These phase space densities reveal three distinct populations of ions in the upstream region: (i) the thin beam of solar wind ions, (ii) a thin beam of reflected ions, extending from 06:02:18 to 06:02:33 UTC, and (iii) the hot, backstreaming ion population visible across the full time interval within the normal velocity range $0 < v_n < 400$ kms^{-1}. These three ion populations are typical of a quasi-parallel shock, though reflection of ions is likely to be intermittent (Gosling et al., 1989).

2.2. A Rippled Shock Surface

In Figure 2, the phase space density as a function of the normal ion velocity is shown for the time interval 06:02:14 to 06:02:30 UTC, for all four MMS spacecraft. During this period, the spacecraft encounter several holes in the ion phase space with a period of approximately 1.5 s in the first half of the interval, and approximately 3 s in the latter half. These ion phase space holes, visible as deficiencies in the ion phase space density at $v_n \sim -50$ kms^{-1}, are consistent with the spacecraft periodically transitioning between regions dominated by shocked plasma in the overshoot and regions dominated by the near-specularly reflected ions and incoming solar wind ions upstream of the shock. This pattern may be associated with a ripple in the surface of the shock, as previously observed by MMS for a quasi-perpendicular shock (Johlander et al., 2016). Under this

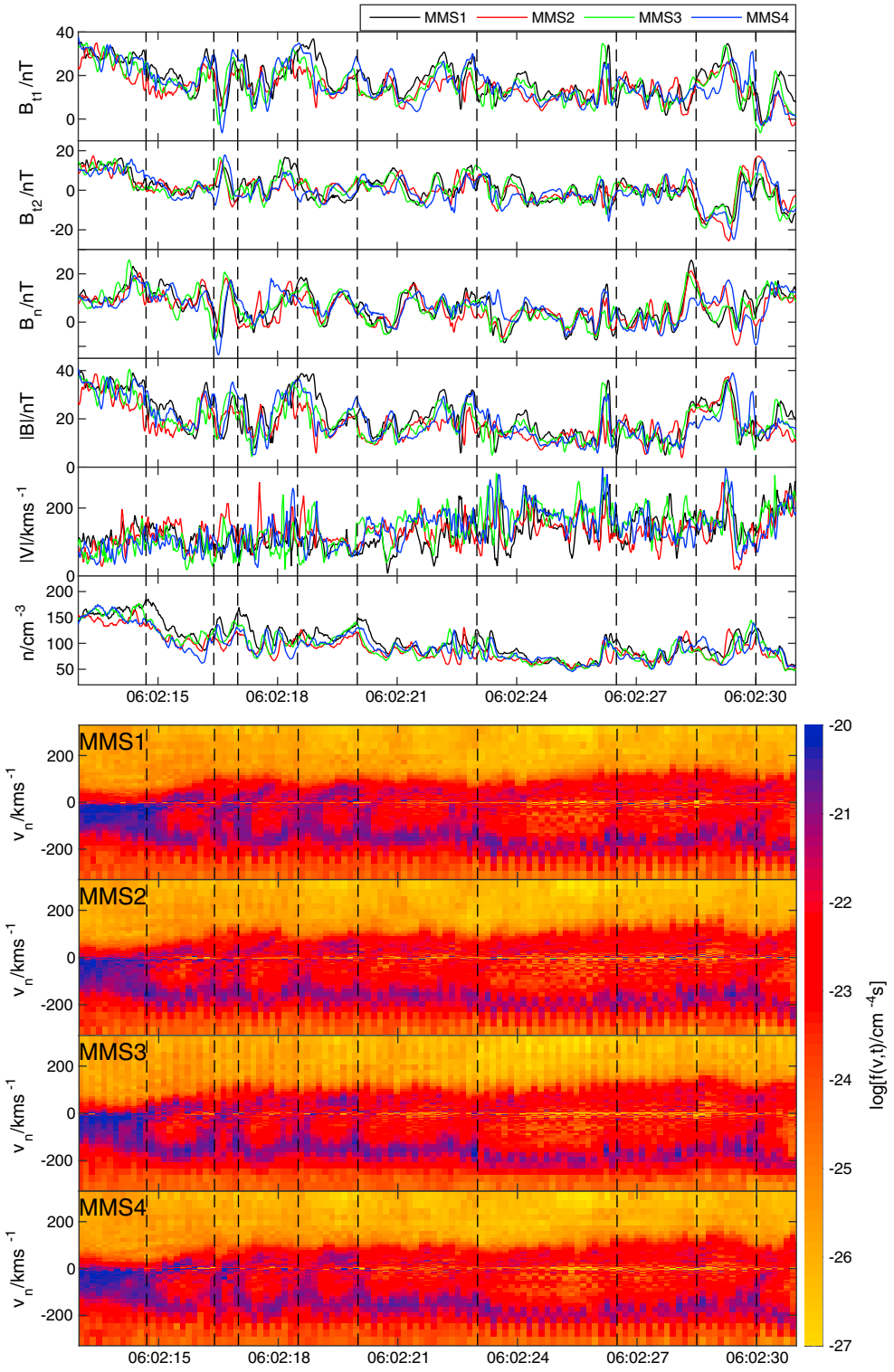


Figure 2. Magnetic fields and ion moments (top) and the phase space density as a function of normal ion velocity (bottom) for the four spacecraft during the period for which ion phase space holes are visible. Dashed lines mark the edges of each phase space hole.

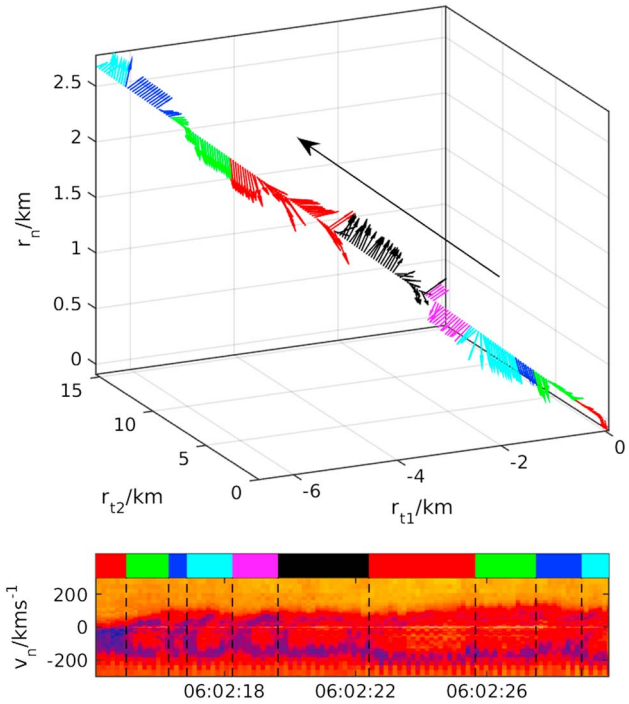


Figure 3. (top) Direction of the local shock normal plotted on the trajectory the MMS1 during the crossing period, in shock normal coordinates. The colors of the arrows correspond to time periods associated with each ion phase space hole. The larger black arrow corresponds to the direction of travel. The viewing angle and unequal axis scales are chosen for clarity. (bottom) The ion phase space density as a function of the normal velocity for MMS1, displaying the time intervals associated with each arrow color.

interpretation, the holes visible in the time series of the ion phase space density (Figure 2) arise from variation in the structure of the shock tangential to its normal. That is, the shock appears to move periodically upstream and downstream as a surface ripple propagates tangentially past the spacecraft.

On crossing a rippled shock surface, an observer would expect to see a periodic oscillation of the normal component of the magnetic field, B_n (Burgess, 2006). This has been demonstrated in observations of a ripple at a quasi-perpendicular shock (Johlander et al., 2016). Although we do observe strong fluctuations in B_n, shown in Figure 2, these fluctuations are not so clearly correlated with the ion phase space holes as in the observed quasi-perpendicular cases. This may be a consequence of the turbulent or unsteady shock foot observed for quasi-parallel shocks (Lucek et al., 2008; Greenstadt et al., 1982). However, we also note that there are clearer correlations between the edges of the phase space holes and peaks in both the magnitude of the magnetic field and the ion density, consistent with a crossing into a compressed overshoot region.

In order to more directly assess the change in direction of the shock surface, we can employ a four-spacecraft timing method over a short section of the time series of length δt, beginning at time t. The local shock normal $\hat{\mathbf{n}}_{sh}(t)$ is given by the solution of the equation (Schwartz, 1998):

$$\begin{pmatrix} \mathbf{\Delta r_{12}} \\ \mathbf{\Delta r_{13}} \\ \mathbf{\Delta r_{14}} \end{pmatrix} \cdot \frac{\hat{\mathbf{n}}_{sh}(t)}{v_{sh}(t)} = \begin{pmatrix} \Delta t_{12}(t) \\ \Delta t_{13}(t) \\ \Delta t_{14}(t) \end{pmatrix}, \tag{1}$$

where $\mathbf{\Delta r_{ij}}$ is the separation of spacecraft i and j, and $\Delta t_{ij}(t)$ is the timing difference found from correlation analysis of B_n for the range $t \rightarrow t + \delta t$. This analysis can be performed for all times t within the selected interval to determine the evolution of the direction of the shock normal. This timing analysis assumes that the relevant structure is planar on the scale of the spacecraft separation Δr_{ij}. The resulting time dependence of $\hat{\mathbf{n}}_{sh}(t)$ is shown for $\delta t = 2$ s in Figure 3, plotted along the trajectory of MMS1 in the large-scale shock coordinate system described by $\hat{\mathbf{t}}_1, \hat{\mathbf{t}}_2, \hat{\mathbf{n}}$. The colors in this figure separate the time series into sections corresponding to each ion phase space hole. It becomes clear from this figure that the phase space holes are strongly correlated with rotations in the local shock normal. The oscillatory change in shock normal direction distinguishes this event from a crossing of successive planar structures. For example, whistler wave-driven instabilities have been shown to generate ion phase space holes (Scholer & Burgess, 2007), but these structures are not accompanied by local deviations of B_n or $\hat{\mathbf{n}}_{sh}$ and are not present in whistler subcritical shocks (here $M_A/M_{cw} = 0.7$). Hence, we can conclude that these observations are consistent with a shock surface ripple propagating past the spacecraft.

We can estimate the properties of this surface ripple by again performing a four-spacecraft timing analysis, as in equation (1), for the full period during which we observe ion phase space holes. In this case, the velocity of the surface ripple is determined to be $v_r = [84, 94, -70]\,\mathrm{kms}^{-1}$ in the spacecraft frame, rotated into shock coordinates $[\hat{\mathbf{t}}_1, \hat{\mathbf{t}}_2, \hat{\mathbf{n}}]$. Accounting for Doppler shift due to the upstream flows, the speed of the ripple is $(\mathbf{v}_r - \mathbf{v}_{sw}) = [1.2, 65, 175]\,\mathrm{kms}^{-1}$. The tangential propagation speed is therefore given by $|(\mathbf{v}_r - \mathbf{v}_{sw}) \cdot \hat{\mathbf{t}}| = 65\ \mathrm{kms}^{-1}$. This corresponds to a speed $\sim 3v_{A,sw}$ in terms of the upstream solar wind Alfvén speed, or $\sim 0.7v_{A,o}$ in the overshoot. For a ripple period of approximately $\Delta t = 1.5$ s, determined by the crossing time for an ion phase space hole, we find that the wavelength of the ripple, given by $\lambda = v_r \Delta t$, is $\lambda \sim 110$ km $\sim 2d_i$, where $d_i = v_{A,sw}/\Omega_i$ is the upstream ion inertial length. In the latter half of the time interval during which we observe ion phase space holes, the period is increased to $\Delta t = 3$ s and hence $\lambda \sim 4d_i$. We can estimate the peak-to-peak amplitude A_r of the ripple given the size of oscillations of the normal field ΔB_n which are associated with ion phase space holes (seen in Figure 2). Under the assumption that the ripples follow a sine wave profile, the amplitude is given by (Johlander et al., 2016)

$$A_r = \frac{\lambda \Delta B_n / B_{0,r}}{\pi \sqrt{4 - \left(\Delta B_n / B_{0,r}\right)^2}}, \tag{2}$$

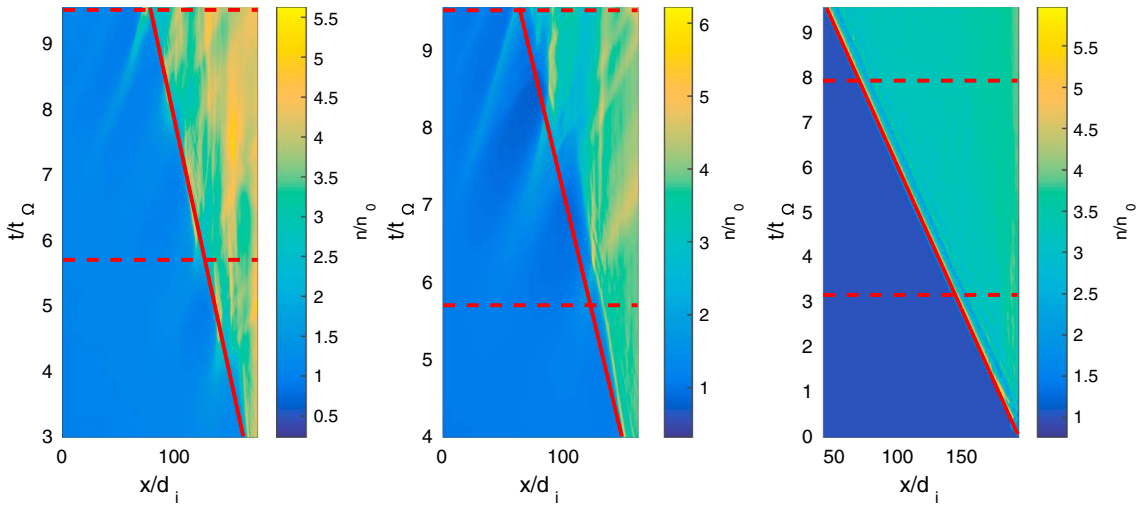


Figure 4. Mean number density, averaged along the tangential y direction, of successive time steps (vertical axis) as a function of x position (horizontal axis) for $\theta_{Bn} = 30°$ (left), $\theta_{Bn} = 40°$ (middle) and $\theta_{Bn} = 60°$ (right). Shock reformation is evident from $t \approx 4t_\Omega$ and $6t_\Omega$ in the 30° and 40° cases, respectively. Red dashed lines mark the periods over which the normal magnetic field is displayed in Figure 5. Red solid lines correspond to the mean shock velocity $< v_{sh} >$ and the position $x_{cut}(t)$ over which the normal magnetic field is displayed in Figure 5.

where $B_{0,r}$ is the local field magnitude. For $\Delta B_n = 20$ nT and $B_{0,r} = 21$ nT, the ripple amplitude is given by $A_r = 19\,\text{km} = 0.4d_i$. The speed, wavelength, and amplitude of these ripples are in agreement with those found in hybrid simulations exhibiting surface ripples (Lowe & Burgess, 2003; Ofman & Gedalin, 2013).

3. Simulations

In order to better understand the form of the rippled shock surface observed by MMS, and the consequences of quasi-parallel and marginally quasi-parallel geometry on ripple development, we conduct hybrid simulations of shocks with a range of angles θ_{Bn}. Winkse and Quest (1988) present an early example. Our chosen hybrid method combines a fully kinetic treatment of the ions with a charge neutralizing, massless, and adiabatic electron fluid. Maxwell's equations are solved in the low-frequency Darwin limit using the CAM-CL algorithm described by Matthews (1994). Here we use the hybrid code HYPSI, as utilized by previous shock studies (Burgess et al., 2015; Sundberg et al., 2016).

The simulations use a grid in (x, y) of size $(L_x, L_y) = (394, 24)d_i$ with resolution $\Delta x = \Delta y = 0.15d_i$ where $d_i = v_{A,sw}/\Omega_i$ is the ion inertial length. The simulations are "2.5D," such that all three components of the fields and moments may vary on the two-dimensional grid, for example, $B_{x,y,z}(x, y, t)$. In the generalized Ohm's law we have used resistivity $\eta = 10^{-2}\mu_0 v_{A,sw}^2/\Omega_i$. Distance and time are normalized to units of the ion inertial length d_i and inverse ion gyrofrequency Ω_i^{-1}, respectively; velocity is normalized to the upstream Alfvén speed $v_{A,sw}$. In order to reduce noise as far as possible given the constraints of the available computational resources, the ion phase space has been sampled with 100 pseudo-particles per computational cell. The boundaries $y = 0, L_y$ are periodic, the boundary $x = L_x$ is reflecting, and the boundary $x = 0$ is a source for inflowing solar wind ions. The initial conditions are homogeneous, with number density $n = n_0$, magnetic field $\mathbf{B}_0 = [B_0 \cos\theta_{Bn}, B_0 \sin\theta_{Bn}, 0]$, and bulk velocity $v_{sw} = [6v_{A,sw}, 0, 0]$. The interaction of the plasma flow in the $+x$ direction with the reflecting boundary generates a shock moving in the $-x$ direction with Mach number $M_A \sim 8$. The ions and electron fluid are initialized with $\beta_{i,e} = 1$. We present three different simulations in this paper, with $\theta_{Bn} = 30°, 40°, 60°$, in order to contrast the behavior of quasi-parallel, marginally quasi-parallel and quasi-perpendicular shocks.

The evolution of the simulations for the three cases is shown in Figure 4. The number density is shown as a function of the shock normal coordinate x and time, averaged over the y direction. The position of the shock is visible as a sharp increase in the number density traveling in the $-x$ direction at approximately $2v_{A,sw}$, indicating that the Mach number of each shock is approximately $M_A \sim 8$. When the shock is far from the reflection boundary and both the upstream and downstream structure are well developed, the $\theta_{Bn} = 30°$ and 40° shocks are seen to begin a periodic reformation cycle. In the marginally quasi-parallel $\theta_{Bn} = 40°$ case,

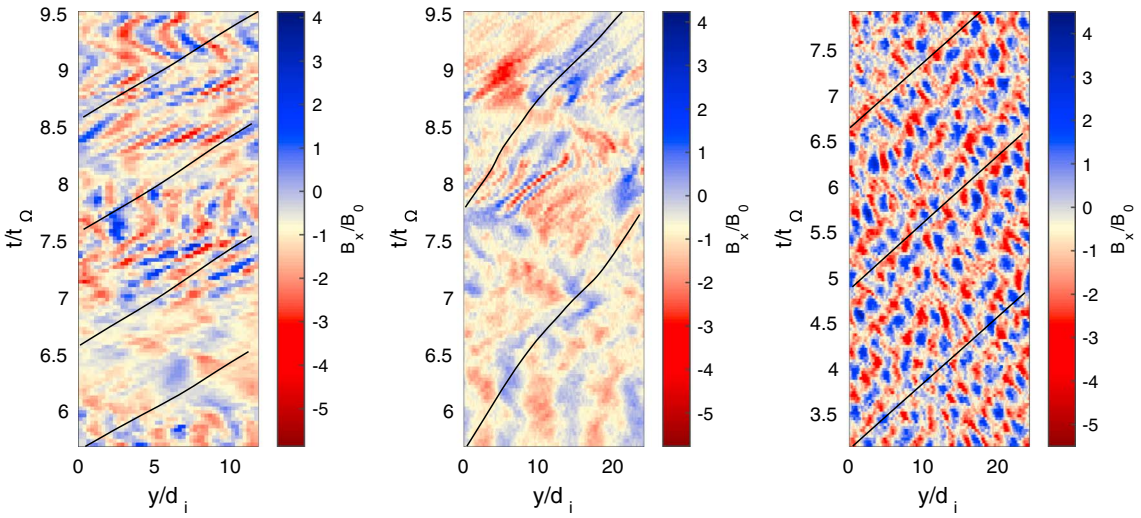


Figure 5. Normal magnetic field $B_x(y,t)$ for $\theta_{Bn} = 30°$ (left), 40° (center), and 60° (right), showing the evolution of the field within a cut along the y direction which moves with the shock front (see Figure 4). Propagating ripples are visible in all cases as structures moving diagonally in the $+y$ direction. Black diagonal lines correspond to the local Alfvén speed within that slice of the simulation and are closely aligned with the speed of the ripples. Note that while in the quasi-perpendicular case the ripple is stable over long periods, in the quasi-parallel and marginally quasi-parallel cases the ripples are transient.

for example, the reformation cycle begins at $t = 6.2t_\Omega$. Upstream of the shock ramp, the influence of the backstreaming ion beam in the foreshock generates a growing upstream wave with downstream-directed group velocity. Within two gyroperiods, this upstream wave steepens and forms a new, fully developed shock ramp. The reformation cycle continues as a second upstream wave begins to grow and steepen at $t \sim 8t_\Omega$. In the quasi-parallel $\theta_{Bn} = 30°$ case, the shock surface is seen to begin its reformation cycle at an earlier time, at $t \sim 4t_\Omega$. Hybrid simulations have demonstrated that upstream plasma parameters may be strongly y dependent (Dubouloz & Scholer, 1995), and therefore reformation processes dependent upon upstream conditions may also be strongly y dependent. In such a case, signatures of reformation may not be visible in the y-averaged plots shown in Figure 4. However, we can confirm that in the quasi-perpendicular case $\theta_{Bn} = 60°$ the upstream conditions do not significantly vary in the tangential direction, and no reformation signatures are visible even in the x-y plane.

To demonstrate the evolution of the magnetic structure in the shock ramp, we present plots of cuts through the simulation in the y direction moving with the shock ramp, that is, $B_x(x = x_{\rm cut}(t), y, t)$. The x position of the cut is given by $x_{\rm cut}(t) = L_x - \langle v_{\rm sh}\rangle t$, where $\langle v_{\rm sh}\rangle = 2.2v_{\rm A,sw}$ for $\theta_{Bn} = 40, 60°$, and $\langle v_{\rm sh}\rangle = 1.8v_{\rm A,sw}$ for $\theta_{Bn} = 30°$. The position of the cuts is shown as a function of time as red lines in Figure 4. We note that the deviation of the red line from the shock at early times $t < 6t_\Omega$ in the $\theta_{Bn} = 40°$ case is due to the change in shock speed observed when the shock reformation cycle begins. In the quasi-parallel cases, the position $x_{\rm cut}$ is chosen to intersect with the regions of the reforming shocks which generate ripples. The x component of the magnetic field along these cuts, shown in Figure 5, reveal several important differences between the quasi-perpendicular and quasi-parallel cases. In the quasi-perpendicular case, a periodic, propagating pattern associated with a shock surface ripple is clearly visible after $t/t_\Omega = 5$. In these figures, the local Alfvén speed is presented as a diagonal black line. This ripple has a tangential speed of $v_r = 1.7v_{\rm A,sw}$, very similar to the local Alfvén speed shown. Given the similarity of this tangential speed to the Alfvén speed in this overshoot, this is consistent with simulations presented in previous literature (Lowe & Burgess, 2003). These patterns provide a clear representation of the influence of a ripple on the local shock structure and can help determine the time periods at which ripples may be seen in simulations which exhibit other sources of nonstationarity. From Figure 5, the wavelength of the ripple is approximately $\lambda_r \sim 5d_i$. The amplitude, determined by examination of the magnetic field strength at the ripple $|B(x,y)|$, is approximately $A_r \sim 1.5d_i$.

In the quasi-parallel $\theta_{Bn} = 30°$ case, the shock begins a repeating reformation cycle after $t \sim 4t_\Omega$. After this time, the shock is sufficiently far from the influence of the reflecting boundary and can be considered well developed. Unlike the $\theta_{Bn} = 60°$ case, surface ripples are not visible at all times. For example, ripples with tangential speed $v_r = 3v_{\rm A,sw}$ can be seen for $7.2 < t/t_\Omega < 7.6$and $8.2 < t/t_\Omega < 8.6$. These transient ripple

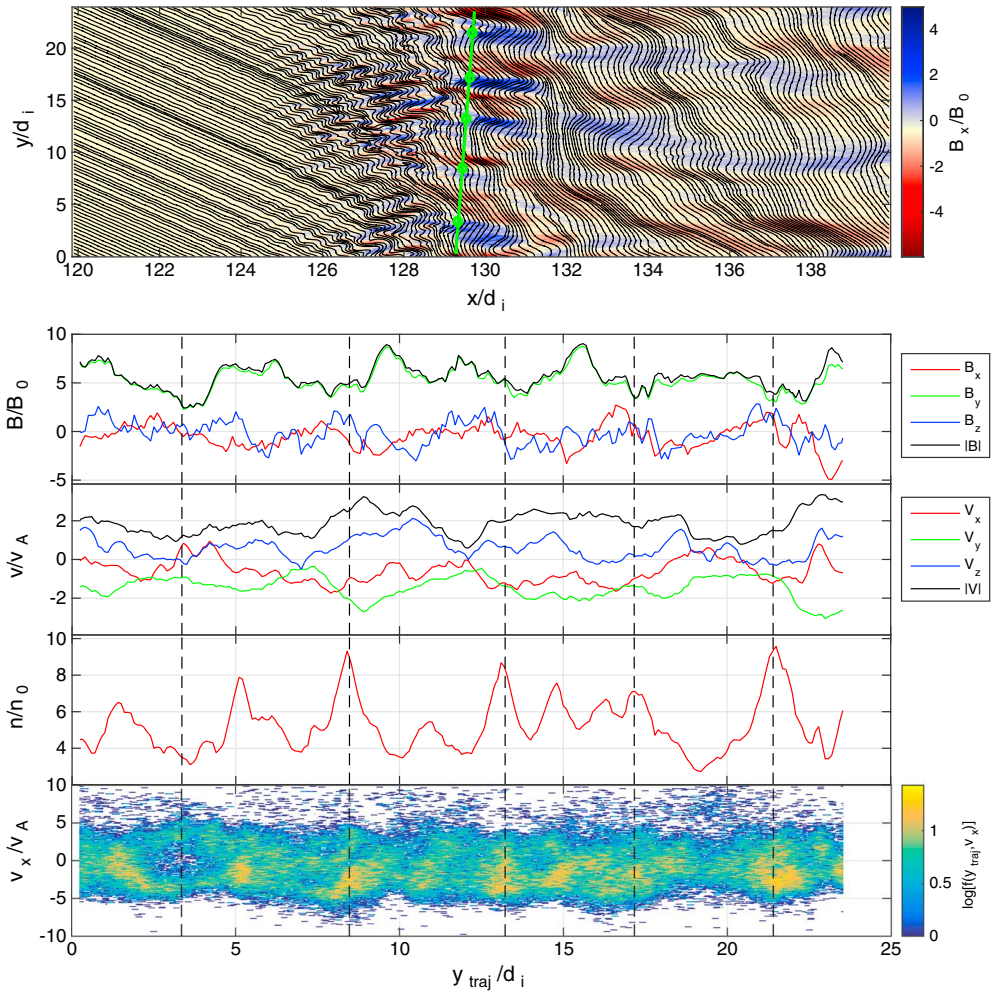


Figure 6. (top) Snapshot of the magnetic structure projected onto the *x*-*y* plane (black lines) and normal field B_x (color) in the *x*-*y* simulation plane for a $\theta_{Bn} = 60°$ shock. (bottom) The magnetic field, velocity field, density, and normal velocity distribution function along the trajectory shown in green. Dashed vertical lines correspond to green circles on the trajectory shown in the top. We note the appearance of a well-formed ion phase space hole at $y_{traj}/d_i = 4$, and a second, less-clear hole at $y_{traj}/d_i = 14$.

signatures again propagate at approximately the local Alfvén speed within the overshoot. In this case, the ripple wavelength and amplitude are given by $\lambda_r \sim 2d_i$ and $A_r \sim 1.5d_i$, respectively.

In the $\theta_{Bn} = 40°$ case, the reformation cycle begins at $t > 6t_\Omega$. Here the ripple signatures in the normal field are not as clear as the coherent structures of the quasi-perpendicular case, nor the transient structures in the quasi-parallel case. However, transient structures with tangential speed $v_r = 3v_{A,sw}$ are visible at $7.6 < t/t_\Omega < 8.3$. A second ripple-like structure with similar speed but longer wavelength is visible at $8.7 < t/t_\Omega < 9.2$. Although the structure of the $\theta_{Bn} = 40°$ simulation more closely resembles the other quasi-parallel case than the quasi-perpendicular case, the less prevalent ripples in the 40° case may be related to the further extension of the foot region downstream of $x_{cut}(t)$ during each reformation cycle. This region is visible in Figure 4 at $x > x_{cut}(t)$. For the $\theta_{Bn} = 40°$ case, the ripple wavelength and amplitude are given by approximately $\lambda_r \sim 3d_i$ and $A_r \sim 1.5d_i$, respectively. This demonstrates the growth of shock surface ripples in simulations for which $\theta_{Bn} < 90°$, in support of the observation discussed in section 2.2 and previous quasi-perpendicular numerical studies (e.g., Yuan et al., 2009). Hence, ripples cannot be considered solely a feature of exactly perpendicular shocks.

Given the time intervals at which we expect to observe a ripple from Figure 5, we more closely examine the shock structure at these times. The stable ripple visible in the $\theta_{Bn} = 60°$ case is shown in Figure 6. In Figure 6 (top), the surface ripple is clear in both the structure of the projected magnetic field and in the normal component of the magnetic field B_x, in color. Several fields and the ion phase space are shown for the trajectory

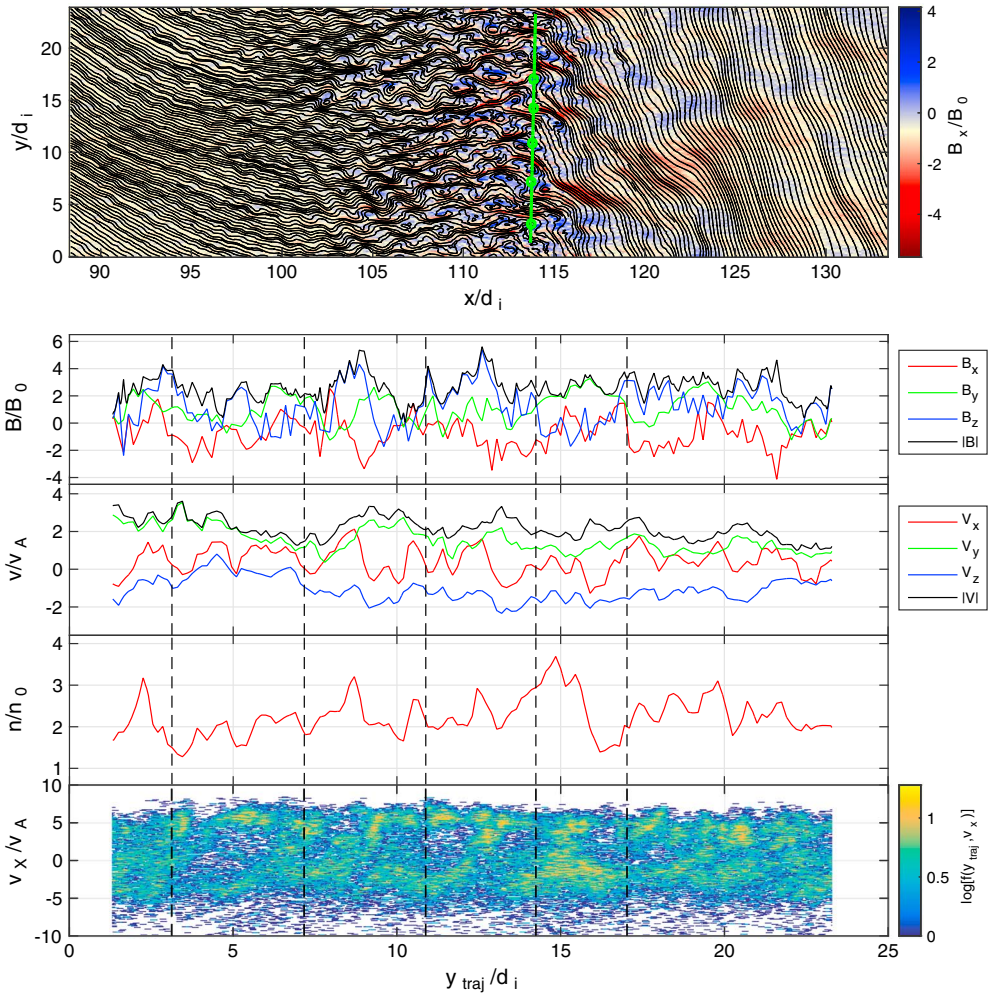


Figure 7. (top) Snapshot of the magnetic structure projected onto in the *x*-*y* plane (black lines) and normal field B_x (color) in a simulation of $\theta_{Bn} = 40°$ shock at $t = 7t_\Omega$. (bottom) The magnetic field, velocity field, density, and normal velocity distribution function along the trajectory shown in green. Dashed vertical lines in the field data correspond to green circles on the trajectory shown in the top. Ion phase space holes are visible at $y_{\text{traj}}/d_i = 5, 11, 14$.

given in green in the Figure 6 (top). We observe oscillations in the normal field B_x consistent with a rippled shock, and peaks in the ion number density and magnetic field strength, consistent with the transition to the compressed overshoot plasma. In Figure 6 (bottom), an ion phase space hole is clearly visible at $y_{\text{traj}}/d_i = 4$. In agreement with Figure 5, the scale length of the phase space holes is approximately $\lambda \sim 5d_i$. In this case, oscillations in the components and magnitude of the bulk velocity are not clearly correlated with other ripple signatures.

A snapshot of the marginally quasi-parallel simulation $\theta_{Bn} = 40°$ is shown in Figure 7. In this case, the apparent growth of turbulence in the immediate upstream region of the shock obfuscates the clear ripple signatures seen for the $\theta_{Bn} = 60°$ case. Furthermore, this simulation exhibits reformation of the shock surface, and ripple-like signatures are only clearly visible during sections of the reformation cycle for which the shock ramp is well developed. From Figure 7 we see that periodic oscillations are visible in the field line structure and normal field B_x. However, they are not as clear as for the quasi-perpendicular case. Importantly, we do find hole-like structures in the ion phase space along the chosen trajectory, on the boundary between the newly developed turbulent upstream region and the reformed shock ramp. We note that these structures are not well resolved in the lower density regions of the ion phase space due to the limitations of sampling the distribution function in a particle in cell code. However, the fields along the trajectory shown in Figure 7 in several ways resemble those seen for the shock crossing observed by MMS in Figure 2. Both display peaks in the ion number density and magnetic field strength correlated with the overshoot-like edges of the ion phase space holes, both

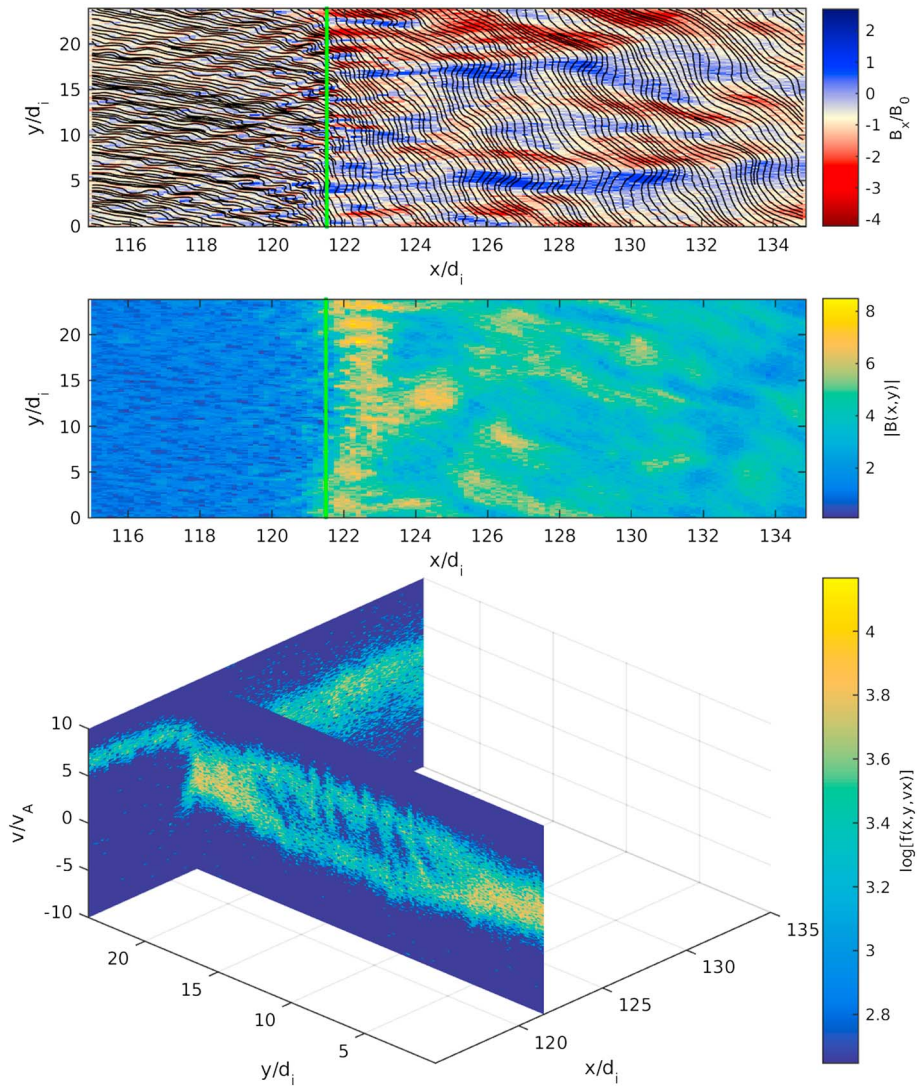


Figure 8. (top) Snapshot of the magnetic structure (black) and normal field B_x (color) for the $\theta_{Bn} = 40°$ simulation at $t = 5t_\Omega$. The green line marks the position $x = 121.5d_i$ of the cut shown in the bottom. (middle) The magnetic field strength $|B(x, y)|$ for this region at the chosen time step. (bottom) Cuts at $x = 121.5d_i$ and $y = 24d_i$ of the ion distribution function $f(x, y, v_x)$, showing several ion phase space holes in the shock ramp.

display no clear correlations with the components of the bulk velocity, and both have a visible, if obfuscated, oscillation in the normal component of the magnetic field.

A clearer representation of the appearance of holes in the ion phase space is shown in Figure 8. Cuts through the ion distribution function $f(x, y, v_x)$ show periodic hole-like structures confined to the shock ramp. This cut intersects with a ripple in the field line structure in the overshoot, as seen in Figure 8. A larger-scale trend resembling a phase space hole with wavelength $24d_i$ is also visible. However, the scale of this feature is likely a consequence of the limitations imposed by the size of the simulation box. It is important to note that the phase space holes visible in Figures 6–8 are caused by nonplanar shock structure in the tangential y direction, rather than structural variations in the normal x direction or in time. As such, appearance of these structures is strongly dependent on the chosen cut through the simulation. Equivalently, the appearance of ion phase space holes in time series of the ion phase density, as in Figure 2, is strongly dependent on the trajectory of the spacecraft through the shock. In order to observe this phenomenon, a spacecraft must have significantly different tangential velocity to that of the propagating ripple and spend sufficient time close to the shock ramp that multiple ripple peaks and troughs propagate past it.

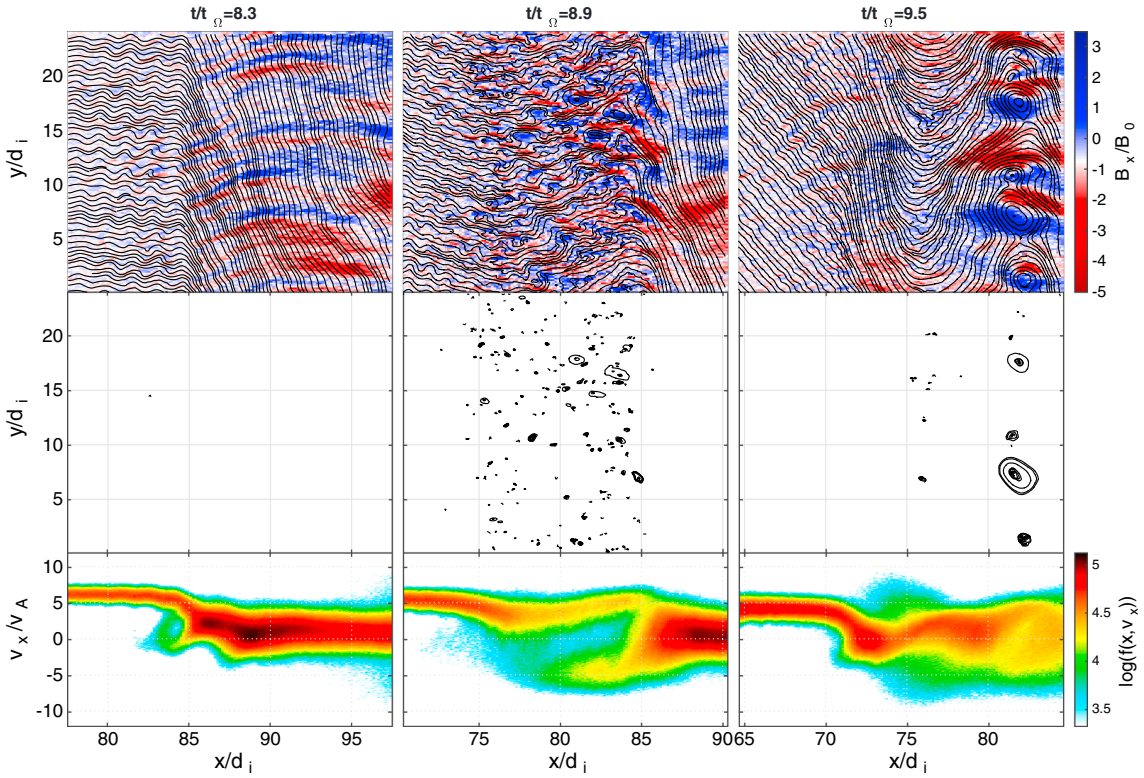


Figure 9. (top) The in-plane field lines (black) and normal component of the magnetic field (color) of time steps of the $\theta_{Bn} = 40°$ hybrid simulation corresponding to different phases of the reformation cycle. (middle) The in-plane magnetic structure as in the top, showing only the field lines wholly closed within the simulation box, that is, those associated with magnetic islands. (bottom) Ion distributions $f(x, v_x)$ as a function of the normal velocity and position, shown for the full range $0 < y/d_i < 24$ for each given time step.

4. Discussion

We have shown using simulations that a fast, propagating ripple can form on a quasi-parallel or marginally quasi-parallel shock, with wavelength on the order of several ion inertial lengths and tangential speed on the order of the overshoot Alfvén speed, consistent with the observed ripple properties determined in section 2.2. However, we have also found that for shocks of this kind, we expect temporal evolution of the shock structure over a time scale of approximately two ion gyroperiods. For the shock observed by MMS, the ion gyroperiod is $t_\Omega \sim 13.2s$, and we therefore expect the shock to have partially reformed over the 16 s period we observe ion phase space holes. Hence, we must examine in more detail how the local shock structure changes during each reformation, in order to determine how that will affect the observations.

Snapshots of the major stages of the reformation cycle are shown for the marginally quasi-parallel ($\theta_{Bn} = 40°$) case in Figure 9. Each panel, from left to right, corresponds to stages 1 to 3 in the following list:

1. A high density of back-streaming ions in the upstream region causes the development of a new shock ramp upstream of the current shock ramp. The new, young shock ramp has a thin compression region and exhibits a *near*-specularly reflected ion population. A ripple develops at the newly formed shock surface. One such newly developed shock is visible in Figure 9 (left column). The oscillation of the normal magnetic field in the transition layer ($x/d_i \sim 85$), visible in color as red and blue alternating bands, illustrates the presence of a ripple at this time step. The tangential propagation of these ripples is shown in Figure 5. We note that in the region in which the ripple develops, the local magnetic field is quasi-perpendicular to the shock normal. Importantly, the growth of this ripple occurs over a time scale much shorter than the ion gyroperiod, implying that the underlying mechanism is not dependent upon the return of reflected ions to the shock surface as they gyrate in the upstream magnetic field.
2. The shock foot develops a turbulent transition region, visible in Figure 9 (top row, middle) for $75 < x/d_i < 85$. Many small magnetic islands have developed within this region, which are shown separately in Figure 9 (middle row). In this step, the red-blue signature of the ripple in the normal field is no longer visible across

the full surface of the shock. In those regions where a ripple may still be present, it appears to be a longer wavelength than the previous snapshot. Within the turbulent region $75 < x/d_i < 85$, the distribution of normal ion velocities (Figure 9, bottom row, middle) broadens for both the incident solar wind and reflected ion population. This heating may be associated with transient reconnection, indicated by the change in topology necessary to develop magnetic islands in the turbulent transition layer (Matsumoto et al., 2015). We note that these islands may only appear with the restriction of the simulations to two dimensions. Further study of the phenomenon will require fully three-dimensional treatments.

3. A new shock ramp forms upstream, at $x/d_i = 72$ in Figure 9 (right column). The turbulent magnetic islands in the older shock ramp have coalesced, as shown in Figure 9 (right column, middle), and have traveled downstream in the shock frame, visible at $x/d_i = 83$. No incoming or reflected ions can be observed close to the older shock ramp, and no ion phase space holes can be observed.
4. A ripple develops at the newly developed shock ramp as in stage 1.

Given that this cycle occurs over two gyroperiods, we expect that the shock observed by MMS will have completed a full reformation cycle during the 30 s period over which we observe reflected ions. Hence, we would expect to observe changes in the ripple properties and eventual loss of the ripple signatures even when the spacecraft is still within the shock ramp and foot. Indeed, the ion phase space density as a function of the normal velocities, shown in Figure 2, reveals a lengthening of the period of the ion phase space holes in the later half of the crossing (from 06:02:23 UTC) to approximately $\Delta t \sim 3$ s. However, the magnitude of the correlated peaks in the magnetic field strength has not reduced during this time. This suggests that the spacecraft have not yet traveled far upstream of the shock and therefore that changes in the properties of the ripples are not merely due to distance from the shock ramp but temporal evolution of the shock surface.

Using MMS, we have identified a marginally quasi-parallel shock ($\theta_{Bn} \sim 42°$) which exhibits signatures in ion phase space consistent with a nonstationary shock surface. In particular, the observation of holes in the ion phase space density and a locally oscillating shock normal indicate the presence of a propagating ripple in the shock surface. These short-scale propagating ripples have been typically associated with quasi-perpendicular shock, both in simulations (Lowe & Burgess, 2003) and observations (Johlander et al., 2016; Moullard et al., 2006). However, we must now consider their appearance in marginally quasi-parallel and quasi-parallel shocks.

Two-dimensional hybrid simulations have shown that surface ripples are present for marginally quasi-parallel and quasi-parallel shocks for the given solar wind conditions. However, unlike ripples in quasi-perpendicular shocks which are coherent over long time periods under the solar wind conditions discussed here, ripples in marginally quasi-parallel and quasi-parallel shocks have been shown to be transient phenomena, modulated by the periodic reformation of the shock surface over time scales on the order of the ion gyroperiod. However, despite these differences in the time scales over which ripples are observable, we note that there are significant structural similarities between the quasi-parallel and quasi-perpendicular cases. Perhaps most importantly, ripples in the quasi-parallel simulations grow and propagate in regions where the local magnetic field is quasi-perpendicular to the shock normal. Hence, the growth of propagating ripples can still be considered a quasi-perpendicular phenomenon.

The time scale over which we observe ion phase space holes in the data has been shown to be approximately the same as the expected reformation period. Indeed, we have observed changes in the properties of the ripples as the spacecraft pass upstream. In this case, we observe an increase in the wavelength of the ripples toward the end of the crossing period. Using comparisons to our simulations of ripples at quasi-parallel and marginally quasi-parallel shocks, we argue that the change in properties of the ripple is associated with the development of a turbulent upstream region, and therefore a lack of a coherent reflection boundary, in the middle of a reformation cycle.

This study underlines the importance of considering different sources of nonstationarity in shock crossings. Here the combination of surface ripple and cyclic reformation make it challenging to separate time and space dependence of shock structure. We have employed a combined approach to the analysis, in which observations and simulations play an important role in interpreting the data, when each separately are not sufficient to characterize the shock crossing. For example, the observations suggest that the ripple propagates in both the $\hat{\mathbf{t}}_1$ and $\hat{\mathbf{t}}_2$ directions, whereas simulations of the ripple phenomena, including those used in this study, are typically 2.5D. Although progress has been made with three-dimensional simulation of quasi-perpendicular

shocks (Burgess et al., 2015), for future efforts in understanding quasi-parallel shock structure we also urge a fully three-dimensional approach.

Finally, the discovery of a transient ripple at a marginally quasi-parallel or quasi-parallel shock may have consequences for the characterization of particle acceleration and heating. A ripple may already introduce a modulation of ion heating and electron acceleration in the shock ramp due to local deviations of the magnetic and electric field direction and magnitude. The observed transience of ripples for $\theta_{Bn} < 45°$ suggests that any steady state treatment of particle acceleration by ripples is likely to incorrectly estimate acceleration and heating.

Acknowledgments
This work was supported by the UK Science and Technology Facilities Council (STFC) grant ST/N000692/1 and grant ST/P000622/1 (D. Burgess). Data used in this research are publically available at the MMS Science Data Center at the Laboratory for Atmospheric and Space Physics (LASP) hosted by the University of Colorado, Boulder (https://lasp.colorado.edu/mms/sdc/public/). We also acknowledge use of NASA/GSFC's Space Physics Data Facility's OMNIWeb service, and OMNI data (https://omniweb.gsfc.nasa.gov/). Simulation data are available upon request (i.gingell@imperial.ac.uk).

References

Abraham-Shrauner, B. (1972). Determination of magnetohydrodynamic shock normals. *Journal of Geophysical Research*, *77*, 736. https://doi.org/10.1029/JA077i004p00736

Auer, P. L., Hurwitz Jr., H., & Kilb, R. W. (1962). Large-amplitude magnetic compression of a collision-free plasma. II. Development of a thermalized plasma. *Physics of Fluids*, *5*, 298–316. https://doi.org/10.1063/1.1706615

Biskamp, D., & Welter, H. (1972). Structure of the Earth's bow shock. *Journal of Geophysical Research*, *77*, 6052–6059. https://doi.org/10.1029/JA077i031p06052

Burch, J. L., Moore, T. E., Torbert, R. B., & Giles, B. L. (2016). Magnetospheric multiscale overview and science objectives. *Space Science Reviews*, *199*, 5–21. https://doi.org/10.1007/s11214-015-0164-9

Burgess, D. (1989). Cyclic behavior at quasi-parallel collisionless shocks. *Geophysical Research Letters*, *16*, 345–348. https://doi.org/10.1029/GL016i005p00345

Burgess, D. (1995). Foreshock-shock interaction at collisionless quasi-parallel shocks. *Advances in Space Research*, *15*, 159–169. https://doi.org/10.1016/0273-1177(94)00098-L

Burgess, D. (2006). Interpreting multipoint observations of substructure at the quasi-perpendicular bow shock: Simulations. *Journal of Geophysical Research*, *111*, A10210. https://doi.org/10.1029/2006JA011691

Burgess, D., Hellinger, P., Gingell, I., & Trávníček, P. M. (2015). Microstructure in two- and three-dimensional hybrid simulations of perpendicular collisionless shocks. *Journal of Plasma Physics*, *82*, 905820401. https://doi.org/10.1017/S0022377816000660

Burgess, D., & Scholer, M. (2015). *Collisionless shocks in space plasmas: Structure and accelerated particles*. Cambridge: Cambridge University Press.

Dubouloz, N., & Scholer, M. (1995). Two-dimensional simulations of magnetic pulsations upstream of the Earth's bow shock. *Journal of Geophysical Research*, *100*, 9461–9474. https://doi.org/10.1029/94JA03239

Gosling, J. T., & Robson, A. E. (1985). Ion reflection, gyration, and dissipation at supercritical shocks. *Washington DC American Geophysical Union Geophysical Monograph Series*, *35*, 141–152. https://doi.org/10.1029/GM035p0141

Gosling, J. T., & Thomsen, M. F. (1985). Specularly reflected ions, shock foot thicknesses, and shock velocity determinations in space. *Journal of Geophysical Research*, *90*, 9893–9896. https://doi.org/10.1029/JA090iA10p09893

Gosling, J. T., Thomsen, M. F., Bame, S. J., & Russell, C. T. (1989). Ion reflection and downstream thermalization at the quasi-parallel bow shock. *Journal of Geophysical Research*, *94*, 10,027–10,037. https://doi.org/10.1029/JA094iA08p10027

Greenstadt, E. W., Hoppe, M. M., & Russell, C. T. (1982). Large-amplitude magnetic variations in quasi-parallel shocks—Correlation lengths measured by ISEE 1 and 2. *Geophysical Research Letters*, *9*, 781–784. https://doi.org/10.1029/GL009i007p00781

Hada, T., Oonishi, M., Lembège, B., & Savoini, P. (2003). Shock front nonstationarity of supercritical perpendicular shocks. *Journal of Geophysical Research*, *108*, 1233. https://doi.org/10.1029/2002JA009339

Hao, Y., Lu, Q., Gao, X., & Wang, S. (2016). Ion dynamics at a rippled quasi-parallel Shock: 2D hybrid simulations. *Astrophysical Journal*, *823*, 7. https://doi.org/10.3847/0004-637X/823/1/7

Johlander, A., Schwartz, S. J., Vaivads, A., Khotyaintsev, Y. V., Gingell, I., Peng, I. B., … Burch, J. L. (2016). Rippled quasiperpendicular shock observed by the magnetospheric multiscale spacecraft. *Physical Review Letters*, *117*(16), 165101. https://doi.org/10.1103/PhysRevLett.117.165101

King, J. H., & Papitashvili, N. E. (2005). Solar wind spatial scales in and comparisons of hourly Wind and ACE plasma and magnetic field data. *Journal of Geophysical Research*, *110*, A02104. https://doi.org/10.1029/2004JA010649

Krauss-Varban, D., & Omidi, N. (1991). Structure of medium Mach number quasi-parallel shocks: Upstream and downstream waves. *Journal of Geophysical Research*, *96*, 17,715–17,731. https://doi.org/10.1029/91JA01545

Lobzin, V. V., Krasnoselskikh, V. V., Bosqued, J.-M., Pinçon, J.-L., Schwartz, S. J., & Dunlop, M. (2007). Nonstationarity and reformation of high-Mach-number quasiperpendicular shocks: Cluster observations. *Geophysical Research Letters*, *34*, L05107. https://doi.org/10.1029/2006GL029095

Lowe, R. E., & Burgess, D. (2003). The properties and causes of rippling in quasi-perpendicular collisionless shock fronts. *Annales Geophysicae*, *21*, 671–679. https://doi.org/10.5194/angeo-21-671-2003

Lucek, E. A., Horbury, T. S., Dandouras, I., & Rème, H. (2008). Cluster observations of the Earth's quasi-parallel bow shock. *Journal of Geophysical Research*, *113*, A07S02. https://doi.org/10.1029/2007JA012756

Matsumoto, Y., Amano, T., Kato, T. N., & Hoshino, M. (2015). Stochastic electron acceleration during spontaneous turbulent reconnection in a strong shock wave. *Science*, *347*, 974–978. https://doi.org/10.1126/science.1260168

Matthews, A. P. (1994). Current Advance Method and Cyclic Leapfrog for 2D Multispecies Hybrid Plasma Simulations. *Journal of Computational Physics*, *112*, 102–116. https://doi.org/10.1006/jcph.1994.1084

Mazelle, C., Lembège, B., Morgenthaler, A., Meziane, K., Horbury, T. S., Génot, V., … Dandouras, I. (2010). Self-reformation of the quasi-perpendicular shock: CLUSTER observations. *Twelfth International Solar Wind Conference*, *1216*, 471–474. https://doi.org/10.1063/1.3395905

Morse, D. L., Destler, W. W., & Auer, P. L. (1972). Nonstationary behavior of collisionless shocks. *Physical Review Letters*, *28*, 13–16. https://doi.org/10.1103/PhysRevLett.28.13

Moullard, O., Burgess, D., Horbury, T. S., & Lucek, E. A. (2006). Ripples observed on the surface of the Earth's quasi-perpendicular bow shock. *Journal of Geophysical Research*, *111*, A09113. https://doi.org/10.1029/2005JA011594

Ofman, L., & Gedalin, M. (2013). Rippled quasi-perpendicular collisionless shocks: Local and global normals. *Journal of Geophysical Research: Space Physics*, *118*, 5999–6006. https://doi.org/10.1002/2013JA018780

Peredo, M., Slavin, J. A., Mazur, E., & Curtis, S. A. (1995). Three-dimensional position and shape of the bow shock and their variation with Alfvenic, sonic and magnetosonic Mach numbers and interplanetary magnetic field orientation. *Journal of Geophysical Research*, *100*, 7907–7916. https://doi.org/10.1029/94JA02545

Pollock, C., Moore, T., Jacques, A., Burch, J., Gliese, U., Saito, Y., … Zeuch, M. (2016). Fast plasma investigation for magnetospheric multiscale. *Space Science Reviews*, *199*, 331–406. https://doi.org/10.1007/s11214-016-0245-4

Russell, C. T., Anderson, B. J., Baumjohann, W., Bromund, K. R., Dearborn, D., Fischer, D., … Richter, I. (2016). The magnetospheric multiscale magnetometers. *Space Science Reviews*, *199*, 189–256. https://doi.org/10.1007/s11214-014-0057-3

Scholer, M., & Burgess, D. (2007). Whistler waves, core ion heating, and nonstationarity in oblique collisionless shocks. *Physics of Plasmas*, *14*(7), 72,103. https://doi.org/10.1063/1.2748391

Scholer, M., Shinohara, I., & Matsukiyo, S. (2003). Quasi-perpendicular shocks: Length scale of the cross-shock potential, shock reformation, and implication for shock surfing. *Journal of Geophysical Research*, *108*, 1014. https://doi.org/10.1029/2002JA009515

Schwartz, S. J. (1998). Analysis methods for multi-spacecraft data. *ISSI Scientific Reports Series*, *1*, 249.

Schwartz, S. J., Thomsen, M. F., & Gosling, J. T. (1983). Ions upstream of the earth's bow shock—A theoretical comparison of alternative source populations. *Journal of Geophysical Research*, *88*, 2039–2047. https://doi.org/10.1029/JA088iA03p02039

Sundberg, T., Haynes, C. T., Burgess, D., & Mazelle, C. X. (2016). Ion acceleration at the quasi-parallel bow shock: Decoding the signature of injection. *Astrophysical Journal*, *820*, 21. https://doi.org/10.3847/0004-637X/820/1/21

Torbert, R. B., Russell, C. T., Magnes, W., Ergun, R. E., Lindqvist, P.-A., LeContel, O., … Lappalainen, K. (2016). The FIELDS instrument suite on MMS: Scientific objectives, measurements, and data products. *Space Science Reviews*, *199*, 105–135. https://doi.org/10.1007/s11214-014-0109-8

Umeda, T., Yamao, M., & Yamazaki, R. (2009). Electron acceleration at a low Mach number perpendicular collisionless shock. *Astrophysical Journal*, *695*, 574–579. https://doi.org/10.1088/0004-637X/695/1/574

Winkse, D., & Quest, K. B. (1988). Magnetic field and density fluctuations at perpendicular supercritical collisionless shocks. *Journal of Geophysical Research*, *93*, 9681–9693. https://doi.org/10.1029/JA093iA09p09681

Yang, Z. W., Lembège, B., & Lu, Q. M. (2012). Impact of the rippling of a perpendicular shock front on ion dynamics. *Journal of Geophysical Research*, *117*, A07222. https://doi.org/10.1029/2011JA017211

Yuan, X., Cairns, I. H., Trichtchenko, L., Rankin, R., & Danskin, D. W. (2009). Confirmation of quasi-perpendicular shock reformation in two-dimensional hybrid simulations. *Geophysical Research Letters*, *36*, L05103. https://doi.org/10.1029/2008GL036675

Erratum

In the originally published version of this article, the acronym THEMIS was misidentified as Thermal Emission Imagining System. This error has since been corrected, and the present version may be considered the authoritative version of record.